Letter   Editors' Suggestion

Marangoni vortex rings in miscible spreading

Anurag Pant and Baburaj. A Puthenveettil

Department of Applied Mechanics, Indian Institute of Technology Madras, Chennai 600036, India

We present the observation of an expanding vortex ring below a fast-spreading ethanol-water film over a deep substrate of water. The radius of the vortex ring (r_v) is shown to scale with time as $t^{1/2}$. The outer radius of the disturbed region (r_o), which comprises the expanding film of length r_f and the plume of length l_p at its periphery, scales in the same way as r_v. Based on this observation, contrary to the earlier proposal of the origin of such vortex rings to be due to evaporative cooling, we hypothesize that such vortex rings occur due to the separation of the shear layer below the plumes. Based on this hypothesis, we obtain scaling laws for the radius of the vortex ring (r_v) and its radial expansion velocity (U_v). These scaling laws are shown to match our measurements, thereby validating the phenomenology of such vortex rings.

Introduction. When an ethanol-water droplet is gently placed on a deep water layer, a fascinating series of phenomena occur due to surface tension driven spreading. A film quickly spreads radially from the drop, while the lighter drop remains at the center. The film then becomes unstable in the azimuthal direction and produces evenly spaced plume-like structures on its outer edge (Movie M1 in the Supplemental Material S5 [1]). Shortly after the appearance of these plumes, the film stops spreading and begins to retract. Eventually, the drop at the center of the film completely mixes with the water as the retraction process concludes; all of these phenomena take less than 0.6 s to complete. Such fast, miscible, surface tension driven film occurs in a variety of fields, including drug delivery, controlling oil spills, coating processes, and ink-jet printing [2–7]. Understanding the involved phenomenon helps in the ability to control and manipulate such spreading in a range of industries. Even though the spreading of such films when their viscosity difference from that of the substrate is large is well understood [8–18], when the film is volatile and miscible, in addition to being slightly more viscous than the substrate and spreading on deep layers, different phenomena and scaling laws have been observed [7,11]. Against the usual $t^{3/4}$ scaling of the spreading radius [8], the film in such cases has been shown to spread as $t^{1/4}$[7], while the length of unstable plumes at the outer periphery of the film scales as $t^{3/4}$[11]. One of the phenomena in such films that is not clearly understood is the presence of a radially expanding vortex ring beneath the spreading film, expanding along with the film's leading edge [7,19] (Movie M2 in the Supplemental Material S6 [1]). Understanding the formation of such vortex rings will shed light on the complex phenomenon of interfacial vorticity generation, which even though it has been explored in various studies [20–29] still remains unclear. Since such vortex rings have so far been observed in relatively slow spreading, either due to high viscosity of the films [30,31] or due to confinement [32], slow processes like evaporative cooling and the associated convective instability in substrates have been proposed [30] as the cause for the formation of such vortex rings. However, there has not been any quantitative proof for such a phenomenology. In contrast to these studies, in deep water layers beneath a fast-expanding ethanol film, we observe the generation and the rapid expansion of a vortex ring. The vortex ring appears at around 40 ms at the periphery of the film and expands rapidly along with the film, as long as the film expands, which takes around 0.3–0.4 s. In this paper, we present this observation of a
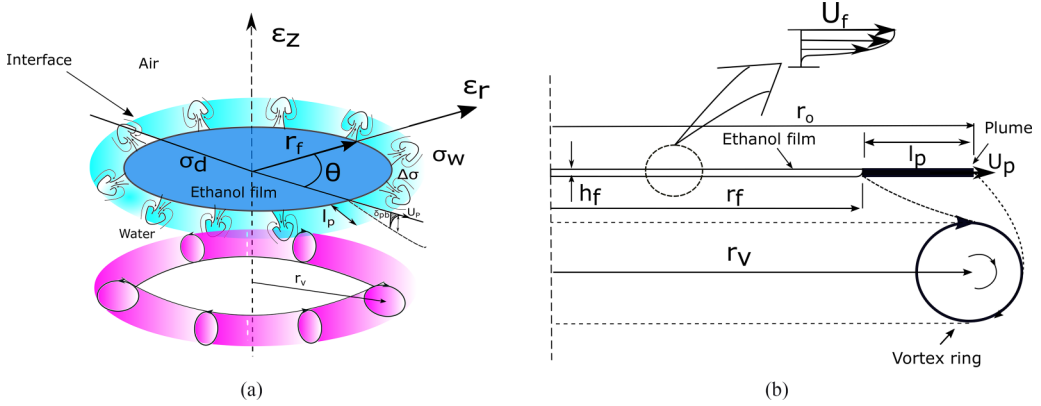
FIG. 1. (a) Schematic of the spreading film, the plumes developing on the film edge, and the vortex ring in the water layer. (b) Schematic of the side view of the film, the plume, and the vortex ring formed due to the separation and roll up of the shear layer.

vortex ring, which is axially stationary but expanding fast radially, below the fast spreading of miscible films (see Fig. 1). Using ethanol-water droplets of size $r_d = 1$ mm and concentrations in the range of $40\% \leqslant C_e \leqslant 100\%$, deposited on the surface of a deep (50-mm) water layer, resulting in density ratios $\chi = \rho_d/\rho_w$ in the range $0.79 < \chi < 0.95$ and viscosity ratios $\xi = \mu_d/\mu_w$ in the range $1.24 < \xi < 2.63$, we make the first quantitative measurements of the variation of the radius (r_v) and the expansion velocities (U_v) of these vortex rings. We then propose a phenomenology, based on shear layer separation, for the origin of these vortex rings. Based on this phenomenology, we obtain scaling laws for the radius and the radial expansion velocity of the vortex ring. A match of these scaling laws with our measurements enhances the plausibility of the proposed phenomenology of these vortex rings.

Experiments; Top-view visualization of the spreading film and the plumes. To visualize the spreading film from the drop at the free surface of the water layer, and its instability at its periphery, high-speed visualizations of aluminum particles spread at the interface were conducted from the top. To ensure that the dynamics at the interface were not affected by the particles, low concentrations (<163 ppm) of particles with a median diameter of 14.65 μm and a mean diameter of 5.09 μm were used. The spreading film was captured in top view using a high-speed camera (Imager Pro HS, LaVision GmbH) with a resolution of 1280×1080 pixels at a frame rate of 800 frames per second (fps). To illuminate the particles, a white light-emitting diode (LED) was used as a backlight. The experiments were conducted in a controlled environment where a temperature of $25\,^{\circ}$C and relative humidity of 40% was maintained (see S1 in Supplemental Material [1] for details of the experimental setup). The images were enhanced by applying a median filter, followed by median background subtraction; details of the image enhancement process are given in S7 in the Supplemental Material [1]. For better visualization of the plume region, images at a particular instant and the nine preceding frames were averaged to create a time-averaged image so that streaks of particle motion are highlighted. Figure 2 shows one such an image, when a drop of radius $r_d = 0.97$ mm and $C_e = 100\%$ was deposited on a 5-mm-deep water layer, with the particle-free region showing the spreading ethanol-water film, and the particle streaks showing the azimuthally distributed plumes at the edge of the film (Movie M1 in the Supplemental Material S5 [1]). The distance of the outermost tips of a few selected plumes from the center was calculated, and an average was taken to determine the mean plume tip radius r_o. Similarly, the distance of the outermost edge of the film was measured at multiple azimuthal locations and averaged to obtain the mean film radius r_f; the mean length of plumes l_p was then calculated as $r_o - r_f$.
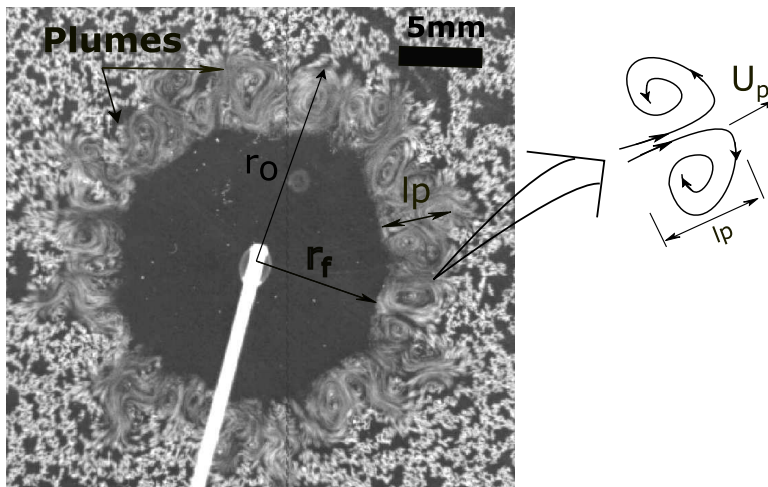
FIG. 2. Top view of the spreading ethanol-water film at the surface of a deep water layer, from a drop of radius $r_d = 0.97$ mm having a concentration of ethanol of $C_e = 100\%$. The image is time averaged over ten frames using instantaneous frames acquired at 800 fps. The schematic shows the circulating flow pattern observed within the plumes.

Particle image velocimetry experiments. We use particle image velocimetry (PIV) from the side to detect the expanding vortex ring below the plumes. PIV experiments were conducted in a glass tank of size 100 mm × 100 mm × 50 mm, filled with water, containing seeding particles (polyamide, 55μ mean diameter, 1.01 g/cm^3 density, Lavision GmbH), up to the brim to avoid meniscus effects. Ethanol-water droplets, with concentrations in the range $40\% \leqslant C_e \leqslant 100\%$, and of size $r_d = 1$ mm, produced by connecting a capillary to a syringe pump were gently deposited at the water surface. The equivalent spherical radius (r_d) was determined by counting the number of droplets that fill a known volume. Table I shows the values of surface tension of the drop fluid with respect to air (σ_d), surface tension difference between the drop fluid and the water layer ($\Delta\sigma$), dynamic viscosities of the drop fluid (μ_d), and densities (ρ_d) of the drop fluid, at various concentrations of ethanol (C_e) in the drops used in our experiments. We used a double-pulsed vertical laser sheet (532 nm, 80 mJ/pulse, Nd:YAG laser, Litron) with a thickness of 1 mm, passed parallel to the tank walls through the center of its cross-sectional area. A high-speed camera (Imager Pro HS, Lavision GmbH) positioned perpendicular to the laser plane captured particle images at 50 Hz. The

TABLE I. Properties of the ethanol-water drops of different concentrations of ethanol (C_e), along with the values of the relevant dimensionless numbers. The properties of the drop at 25 °C were obtained from Ernst *et al.* [33]. For measurements from the visualizations with aluminum particles ($r_d = 0.97$ mm and $C_e = 100\%$), the surface tension values of water were corrected for the decrease caused by the presence of particles on its surface. The table also shows the values of A and B for the best-fit curves of the form $r_v = At^B$ for various C_e.

r_d (mm)	C_e (%)	σ_d (mNm^{-1})	$\Delta\sigma$ (mNm^{-1})	μ_d (cP)	ρ_d (kg m^{-3})	ξ	χ	Oh$_d$ (10^{-3})	A	B
1.00	40	31.00	41.0	2.34	948.47	2.63	0.95	12.0	19.26	0.42
1.00	60	26.00	46.0	2.24	908.72	2.52	0.91	11.0	22.6	0.46
1.00	80	23.80	48.2	1.66	859.58	1.87	0.86	8.2	25	0.40
1.00	100	22.00	50.0	1.10	790.74	1.24	0.79	5.5	30.44	0.41
0.97	100	22.00	32.0	1.10	790.74	1.24	0.79	5.5	39	0.5

(a) 40 ms

(b) 80 ms

(c) 160 ms

(d) 240 ms
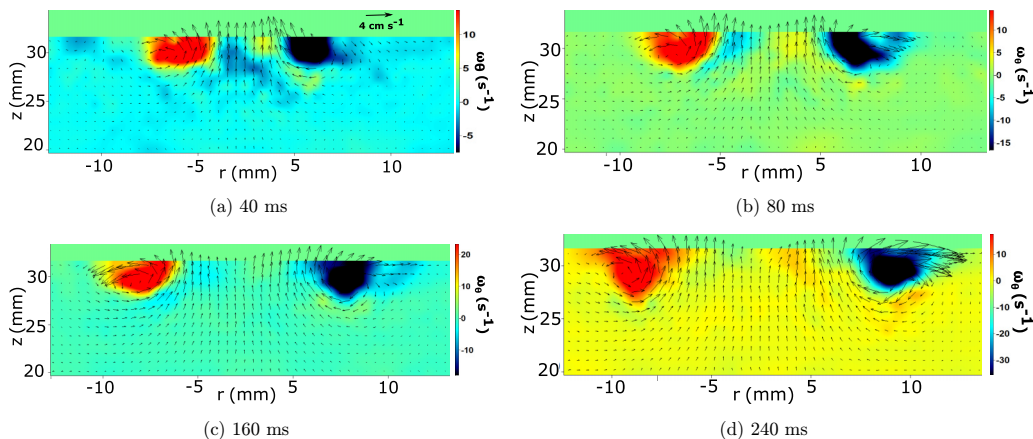
FIG. 3. Instantaneous PIV vector fields, overlaid over the corresponding instantaneous vorticity fields, at different instants during the spreading of the ethanol-water film on the surface of a 50-mm-deep water layer, from an ethanol-water drop of $r_d = 1$ mm having an ethanol concentration $C_e = 80\%$ ethanol (refer to Movie M3 in the Supplemental Material S10 [1] depicting the temporal variation of the vector field).

particle images were processed using an adaptive multipass cross-correlation algorithm that utilizes fast Fourier transform (FFT) in DAVIS 8.4 (Lavision GmbH) (see S1 in the Supplemental Material [1] for details of the PIV). Spurious vectors were detected by fixing a signal-to-noise ratio (SNR) threshold of 1.5, followed by the application of a two-pass median filter in 3×3 neighborhood of each vector (please refer to Section S1 in the Supplemental Material [1] for details on how SNR is estimated, the postprocessing of vectors, and the process for determining uncertainties).

Figure 3 presents the PIV vector fields at different time instants, overlaid over the corresponding vorticity fields, during the spreading of an ethanol film on the surface of a 50-mm-deep water layer, initiated by an ethanol drop with a radius of $r_d = 1$ mm and concentration $C_e = 80\%$. The vorticity field was generated by calculating the circulation along eight vectors surrounding a given vector (see S2 in the Supplemental Material [1] for details on vorticity estimation). Movie M2 in the Supplemental Material S6 [1] shows the corresponding visualization movie of the expansion of the vortex ring. The velocity and the vorticity fields in Fig. 3 show the presence of two counterrotating vortices beneath the spreading ethanol-water film. These counterrotating vortices occur due to the intersection of the laser sheet with an expanding vortex ring below the spreading film, shown schematically in Fig. 1(a). We identify and track the center of these vortices using the λ_2 criterion [34]. Contour plots in Fig. 4(a) depict the variation of λ_2, calculated from the velocity field, at a time instance of $t = 180$ ms after the drop is deposited. Distinct centers for the left and the right vortices that have the highest negative values can be identified from the contour plot of λ_2 (details of the estimation of λ_2 and the process of vortex identification are given in Sec. S3 in the Supplemental Material [1]). Figure 4(b) displays the spatial distribution of the θ component of vorticity (ω_θ) at two different times along the centerline of the vortices. It can be observed that the total vorticity and the peak vorticity increase with time as the vortex ring spreads radially during the course of film spreading. As there is no initial vorticity in the stationary water before drop deposition, the observed increase in vorticity with time implies that there is continuous production of vorticity, possibly due to surface tension gradients at the interface, and its eventual dissipation.

Measurements. Figure 5(a) shows the variation of the radius of the vortex ring $r_v(t)$ measured as the horizontal distance from the point of deposition to the location of maximum negative λ_2 value with time, for various C_e in a drop of $r_d = 1$ mm. The zero time was taken as the time corresponding to the time of contact of the drop with the free surface of the water layer. The first measurement of r_v was made at the instant when the two counterrotating vortices were clearly visible in the vector

(a)

(b)
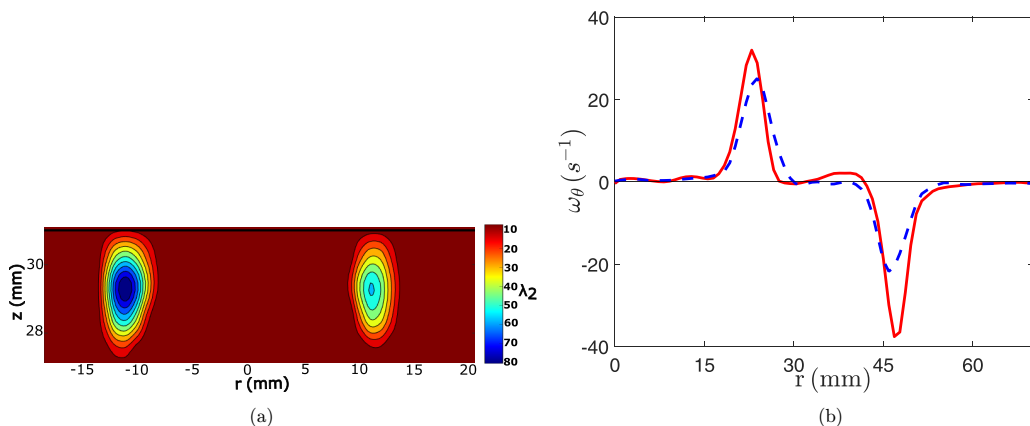
FIG. 4. (a) Contours of λ_2 values obtained from the velocity field at $t = 180$ ms. (b) Variation of the θ component of vorticity (ω_θ) along a horizontal line passing through the vortex centers for $C_e = 80\%$ and $r_d = 1$ mm at $t = 180$ ms (blue dashed line) and $t = 220$ ms (solid red line). The solid line (black) in (a) represents the free surface.

field, and the measurements were limited to the time when the film begins to recede. The error in identifying the center of the vortex using PIV is equal to the width of an interrogation window, which is approximately 16 pixels ≈ 0.90 mm, hence the error in r_v, $\delta r_v = 0.90$ mm. These errors are shown as the error bars in Fig. 5(a). It can be observed from the figure that, at any time instant, a higher C_e corresponds to a higher r_v. The slopes of variation of r_v with t for various C_e are nearly the same, indicating a common $t^{1/2}$ power law dependence of r_v on t for various C_e values, as shown by the dashed line in the figure. The solid square symbols in the figure represent the measured

(a)

(b)
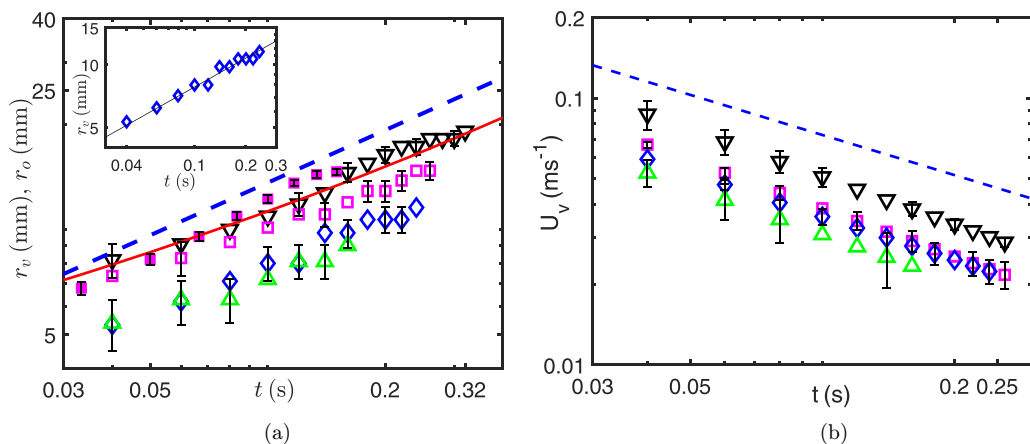
FIG. 5. Variation of (a) the experimentally measured vortex ring radius (r_v) and (b) the mean radial expansion velocity (U_v) of the vortex ring with time (t) for ethanol drops of $r_d = 1$ mm deposited on a 50-mm-deep water layer having the following concentrations of ethanol in the drop: $\triangle$, $C_e = 40\%$; $\diamond$, $C_e = 60\%$; $\square$, $C_e = 80\%$; $\triangledown$, $C_e = 100\%$. The dashed line in (a) shows the scaling $r_v \sim t^{1/2}$, while the solid symbols show the variation of the experimentally measured plume tip radius (r_o) with time for a drop of $C_e = 80\%$ and $r_d = 0.97$ mm, deposited on a 5-mm-deep water layer. The solid line in (a) shows the scaling (10) for a drop of $C_e = 100\%$ and $r_d = 0.97$ mm. The inset in (a) shows r_v vs t for $C_e = 100\%$ and $r_d = 1$ mm, along with the curve fit $r_v = 22.5t^{0.46}$ used for estimating U_v. In (b), the dashed line shows the scaling $U_v \sim t^{-1/2}$.

variation of the mean plume tip radius r_o with time for a drop of $r_d = 0.97$ mm and $C_e = 80\%$. The r_v versus t plots for various concentrations are parallel to the r_o versus t plots for the above case, indicating a similar power law dependence on time. Figure 5(b) illustrates the change in the radial expansion velocity (U_v) of the vortex ring with time for different C_e values. U_v was determined by calculating the slopes of the power law curve fits, of the form $r_v = At^B$, to the r_v versus t data in Fig. 5(a). One such curve fit corresponding to r_v versus t for $C_e = 100\%$ is as shown in the inset of Fig. 5(a). Table I includes the values of A and B obtained from the best-fit curves between r_v and t for different C_e. To calculate the error in U_v, the power law fits were estimated with the maximum and the minimum gradients that would fit the $r_v \pm \delta r_v$ data, where δr_v is 0.9 mm. The gradients of these power law fits gave the maximum and minimum possible values of U_v, which were used to calculate the error δU_v. The resulting values for δU_v are shown in Fig. 5(b) as error bars (see S4 in the Supplemental Material [1] for error analysis). Figure 5(b) indicates that U_v decreases with time as the expanding ethanol film approaches its maximum radius, at which point the spreading of the film ceases, before it starts to retract. Additionally, larger C_e values correspond to larger U_v values at any given time, which suggests that the surface tension gradient has a significant effect on the expansion of the vortex ring.

Scaling Analysis. We now present a scaling analysis for the expanding radius (r_v) of the vortex ring, as well as for its expansion velocity U_v. In our analysis, as the characteristic time of spreading is very small, and since the evaporation velocities are three orders of magnitude smaller than the film velocity (see S8 in the Supplemental Material [1] for details), we assume that the loss of ethanol due to evaporation is negligible and hence the properties of the film remain constant over the short time of spreading. We assume that the expanding vortex ring at the free surface is created by the separation of the shear layer that occurs ahead of the expanding film, below the plumes. This assumption is justifiable since, as shown by Ref. [7], there is no shear layer below the expanding film, with the force due to the radial surface tension gradient at the outer periphery of the film balancing the viscous resistance within the film. However, there is a shear layer below the plumes, as shown by Ref. [11], which is expected to separate at the outer edge of the plumes of radius r_o and roll up into the vortex ring. The expanding vortex ring radius could then be expected to scale as the radius of the outer tips of the plumes, i.e.,

$$r_v(t) \sim r_o(t). \tag{1}$$

Since the plumes originate and grow from the outer periphery of the expanding film,

$$r_o(t) = r_f(t) + l_p(t) \tag{2}$$

at each instant, where r_f is the film radius and l_p the plume length. Equation (1) can then be written as

$$r_v(t) = c_1[r_f(t) + l_p(t)]. \tag{3}$$

The assumption (3) is further justified since r_o exhibits a power law dependence on time that is similar to that observed for the radius of the vortex ring r_v, as shown in Fig. 5(a) (refer to S9 in the Supplemental Material [1] for a comparison of the experimentally measured values of r_f, l_p, and $r_o = r_f + l_p$).

The expression for the film radius r_f in (3), in the case of miscible, volatile ethanol droplets deposited on deep water layers, was obtained by balancing the radial surface tension force between the film and the substrate fluid with the viscous resistance within the film as given by Ref. [7] as

$$r_f = 0.83 \frac{r_d}{f} \left(\frac{t}{t_{\mu d}} \right)^{1/4}, \tag{4}$$

where the viscous-surface tension time scale

$$t_{\mu d} = \frac{\mu_d r_d}{\Delta \sigma}, \tag{5}$$

and the fraction of the drop drawn into the film, as given by Ref. [7], is $G = (3/2^5)f^4$, with

$$f = \frac{3^{1/4}}{2}(1 + \text{Bo}_d)^{7/24},$$ (6)

where the drop Bond number is defined as

$$\text{Bo}_d = \frac{\rho_d g r_d^2}{\Delta \sigma}.$$ (7)

In contrast, as shown by Ref. [11], the plume lengths were obtained by a balance of the surface tension force across the plumes with the viscous resistance of a shear layer below the plumes as

$$l_p = 0.11 r_d \left(\frac{t}{t_\xi}\right)^{3/4},$$ (8)

where the time scale

$$t_\xi = \left(\frac{r_d^4 \rho_w \mu_w}{\Delta \sigma^2}\right)^{1/3}.$$ (9)

Substituting the expressions (4), (5), (8), and (9) in (3), we obtain the radius of the vortex ring as

$$r_v = c_1 \left[\frac{0.83}{f}\left(\frac{\Delta\sigma r_d^3 t}{\mu_d}\right)^{1/4} + 0.11\left(\frac{\Delta\sigma^2}{\mu_w \rho_w}\right)^{1/4} t^{3/4}\right].$$ (10)

Equation (10) shows that the radius of the vortex ring is a sum of two power laws in time, viz., $t^{3/4}$ and $t^{1/4}$, whose equivalent power law, as we show later, scales as $\sqrt{t}$. In addition, r_v shows complex dependence on $\Delta\sigma$, r_d, and both the droplet and the substrate properties. Figure 5(a) shows the scaling (10) for the case of a drop of $C_e = 100\%$ and $r_d = 0.97$ mm. The scaling is in good agreement with the experimental data.

Normalizing (10) with the drop radius r_d, we obtain

$$r_v^* = \frac{r_v}{r_d} = c_1 \left[\frac{0.83}{f}\left(\frac{t}{t_{\mu d}}\right)^{1/4} + 0.11\left(\frac{t}{t_\xi}\right)^{3/4}\right].$$ (11)

Using (5) and (9) in (11) and taking $t^* = t/t_\xi$, the dimensionless time, as a common factor from the right-hand side, we obtain

$$r_v^* = c_1 t^{*3/4}\left[0.11 + \frac{0.83}{f t^{*3/4}}\left(\frac{t}{t_{\mu d}}\right)^{1/4}\right].$$ (12)

The dimensionless vortex ring radius then scales as

$$r_v^* = c_1 t^{*3/4}\Gamma_1,$$ (13)

where

$$\Gamma_1 = 0.11 + \frac{0.83}{f}\left(\frac{t}{t_{\mu d}}\right)^{1/4}\frac{1}{t^{*3/4}}.$$ (14)

Substituting (4) and (9) in (14) and rearranging, we obtain Γ_1 as

$$\Gamma_1 = 0.11 + \frac{0.83}{f}\frac{1}{\sqrt{t^*(\text{Oh}_d\sqrt{\xi}\chi)^{1/3}}},$$ (15)

where $\xi = \mu_d/\mu_w$ is the viscosity ratio, $\chi = \rho_d/\rho_w$ the density ratio, and $\text{Oh}_d = \mu_d/\sqrt{\rho_d \Delta\sigma r_d}$ the drop Ohnesorge number. Figure 6(a) shows the variation of r_v^*/Γ_1 with t^*, where it can be observed
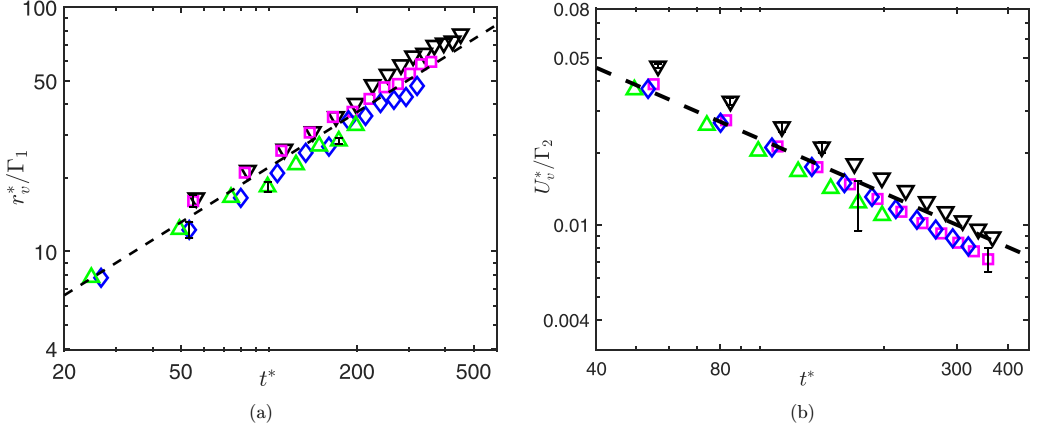
FIG. 6. Scaling of (a) the dimensionless vortex ring radius (r_v^*) (10) normalized by Γ_1(14) and (b) the dimensionless mean radial expansion velocity of the vortex ring (U_v^*) (17) normalized by Γ_2(15) with the dimensionless time ($t^* = t/t_\xi$). The symbols denote r_v^*/Γ_1 and U_v^*/Γ_2 at the following concentrations of ethanol in the drop: $\triangle, C_e = 40\%$; $\diamond, C_e = 60\%$; $\square, C_e = 80\%$; $\triangledown, C_e = 100\%$ for a drop of radius $r_d = 1$ mm. The dashed line in (a) shows the scaling $r_v^*/\Gamma_1 = 0.7t^{*3/4}$, while the dashed line in (b) shows the scaling $U_v^*/\Gamma_2 = 0.72t^{*-3/4}$.

that the data collapses fairly well onto the relation

$$\frac{r_{v^*}}{\Gamma_1} = 0.7t^{*3/4}. \tag{16}$$

Then, the nontrivial scaling given by (13) accurately captures the dependence of the vortex ring radius on time and other drop properties. This match also indicates that the assumption of the vortex ring being generated by the separation of the shear layer below the plumes, so that it expands radially below the plume tip, with the ring radius $r_v \sim r_f + l_p$, is also verified. As shown in Fig. 5(a), the resultant single power-law dependence on time of (13) is $r_v \sim t^{1/2}$.

We can extend the above scaling analysis to obtain the scaling of the dimensionless radial expansion velocity of the vortex ring (U_v^*) as follows. We differentiate (13) with respect to t^* to obtain

$$U_v^* = \frac{U_v}{r_d/t_\xi} = c_1\left(\frac{0.083}{t^{*1/4}} + \frac{0.21}{f}\frac{1}{\sqrt{t^{*3/2}(Oh_d\sqrt{\xi\chi})^{1/3}}}\right), \tag{17}$$

where $U_v = \partial r_v/\partial t$ is the velocity of radial expansion of the vortex ring. Taking the common factor of $1/t^{*3/4}$ outside of the right-hand side of (17), we obtain the dimensionless radial velocity of expansion of the vortex ring as

$$U_v^* = c_1\frac{\Gamma_2}{t^{*3/4}}, \tag{18}$$

where

$$\Gamma_2 = 0.083t^{*1/2} + \frac{0.21}{f}\frac{1}{\sqrt{Oh_d^{1/3}\sqrt{(\chi\xi)^{1/3}}}}. \tag{19}$$

Figure 6(b) shows the variation of U_v^*/Γ_2 with t^*; the data collapses fairly well onto the relation

$$\frac{U_v^*}{\Gamma_2} = 0.72t^{*-3/4}, \tag{20}$$

thereby validating the obtained scaling (18). The scaling given by (18) is a sum of two power-law dependencies on time, namely, $1/t^{1/4}$ and $1/t^{3/4}$; the effective single power law on time seems to scale as $1/t^{1/2}$, as shown in Fig. 6(b). The nontrivial scalings given by (13) and (18) show that, in addition to the surface tension force that drives the film expansion, the drop properties also play an important role in determining the dynamics of the vortex ring, as it expands in the water layer below the expanding film. Furthermore, these scalings justify the assumptions of (i) viscous resistance within the film being the dominant resistance, with no boundary layer being present below the film; (ii) occurrence of a shear boundary layer below the plumes [11], which governs the growth of the plumes; and (iii) the vortex ring being an outcome of the separation of this shear boundary layer.

Conclusions. The outcomes of our study shed light on a particular instance of free surface Marangoni flows, where the interplay of surface tension driven flows and the consequent free surface boundary layer induces intriguing vortical dynamics in the bulk fluid. Our work detects a vortex ring beneath a fast-spreading ethanol-water film, resulting from the gentle deposition of a miscible ethanol-water droplet on the surface of a deep layer of water. The vortex ring is observed to expand along with the film at its periphery, just below the free surface, with the radius of the vortex ring (r_v) expanding with a $t^{1/2}$ power law dependence on time. The expanding film of radius r_f develops azimuthally equally spaced, radially growing plumes, of length l_p, at its periphery; interestingly, the outermost tip radius of the plumes, $r_o = r_f + l_p$, also exhibits the same $t^{1/2}$ power law dependence on time as that of the vortex ring radius. Contrary to the earlier hypothesis of the origin of such vortex rings, which were based on evaporative cooling, based on the observation of the same power law dependence of r_o and r_v, we hypothesize that the vortex ring is an outcome of the separation and roll up of the shear layer below the plumes. Then, by using the scaling relations for r_f [7] and l_p [11], we obtained scaling relations for the vortex ring radius r_v and its radial expansion velocity U_v as functions of time and properties of the droplet and the substrate. These scaling relations matched our measurements of r_v and U_v, thereby validating the hypothesis of the vortex ring being generated by the separation of the shear layer below the plumes.

[1] See Supplemental Material at http://link.aps.org/supplemental/10.1103/PhysRevFluids.9.L012701 for details on top-view visualization, particle image velocimetery experiment, information on tracer particle passiveness, vorticity estimation, vortex core identification, and image enhancement, including a movie of a top-view experiment with an ethanol-water drop deposited on a 5-mm water layer; a movie of side-view visualization with neutrally buoyant particles in water and rhodamine-6g in the drop, a movie showing the evolution of the PIV vector field with time; and a comparative plot showing the film radius, mean plume length, and mean outer tip radius of the film. The Supplemental Material also contains Refs. [7,11,19,35–44].

[2] B. James Grotberg, Pulmonary flow and transport phenomena, Annu. Rev. Fluid Mech. **26**, 529 (1994).

[3] O. E. Jensen and J. B. Grotberg, Insoluble surfactant spreading on a thin viscous film: Shock evolution and film rupture, J. Fluid Mech. **240**, 259 (1992).

[4] H. P. Le, Progress and trends in ink-jet printing technology, J. Imaging Sci. Technol. **42**, 49 (1998).

[5] J. La Due, M. R. Muller, and M. Swangler, Cratering phenomena on aircraft anti-icing films, J. Aircr. **33**, 131 (1996).

[6] J. A. Fay, The spread of oil slicks on a calm sea, in *Oil on the Sea: Proceedings of a Symposium on the Scientific and Engineering Aspects of Oil Pollution of the Sea, Sponsored by Massachusetts Institute of Technology and Woods Hole Oceanographic Institution and Held at Cambridge, Massachusetts, May 16, 1969* (Springer, New York, 1969), pp. 53–63.

[7] R. Dandekar, A. Pant, and B. A. Puthenveettil, Film spreading from a miscible drop on a deep liquid layer, J. Fluid Mech. **829**, 304 (2017).

[8] R. B. J. Koldeweij, B. F. van Capelleveen, D. Lohse, and C. W. Visser, Marangoni-driven spreading of miscible liquids in the binary pendant drop geometry, Soft Matter **15**, 8525 (2019).

[9] A. H. Mollaei and S. Darooneh, Spreading, fingering instability and shrinking of a hydrosoluble surfactant on water, Exp. Therm. Fluid Sci. **86**, 98 (2017).

[10] T. F. Svitova, R. M. Hill, and C. J. Radke, Spreading of aqueous trisiloxane surfactant solutions over liquid hydrophobic substrates, Langmuir **17**, 335 (2001).

[11] A. Pant, B. A. Puthenveettil, and S. K. Kalpathy, Marangoni plumes in miscible spreading, Phys. Fluids **35**, 032107 (2023).

[12] L. Keiser, H. Bense, P. Colinet, J. Bico, and E. Reyssat, Marangoni bursting: Evaporation-induced emulsification of binary mixtures on a liquid layer, Phys. Rev. Lett. **118**, 074504 (2017).

[13] S. M. Troian, X. L. Wu, and S. A. Safran, Fingering instability in thin wetting films, Phys. Rev. Lett. **62**, 1496 (1989).

[14] A. B. Afsar-Siddiqui, B. Abia, P. F. Luckham, and O. K. Matar, The spreading of surfactant solutions on thin liquid films, Adv. Colloid Interface Sci. **106**, 183 (2003).

[15] X. Ma, M. Zhong, Y. He, Z. Liu, and Z. Li, Fingering instability in Marangoni spreading on a deep layer of polymer solution, Phys. Fluids **32**, 112112 (2020).

[16] K. Nagai, Y. Sumino, H. Kitahata, and K. Yoshikawa, Mode selection in the spontaneous motion of an alcohol droplet, Phys. Rev. E **71**, 065301(R) (2005).

[17] A. Mizev, A. Trofimenko, D. Schwabe, and A. Viviani, Instability of Marangoni flow in the presence of an insoluble surfactant. Experiments, Eur. Phys. J.: Spec. Top. **219**, 89 (2013).

[18] A. Mizev, Influence of an adsorption layer on the structure and stability of surface tension driven flows, Phys. Fluids **17**, 122107 (2005).

[19] A. Pant and B. A Puthenveettil, Vortex ring below a spreading alcohol film on water, J. Flow. Vis. Image. Proc. **27**, 219 (2020).

[20] E. P. Rood, Myths, math, and physics of free-surface vorticity, Appl. Mech. Rev. **47**, S152 (1994).

[21] T. Sarpkaya, Vorticity, free surface, and surfactants, Annu. Rev. Fluid Mech. **28**, 83 (1996).

[22] S. Sur, H. Masoud, and J. P. Rothstein, Translational and rotational motion of disk-shaped Marangoni surfers, Phys. Fluids **31**, 102101 (2019).

[23] M. Brøns, M. C. Thompson, T. Leweke, and K. Hourigan, Vorticity generation and conservation for two-dimensional interfaces and boundaries, J. Fluid Mech. **758**, 63 (2014).

[24] R. W. Cresswell and B. R. Morton, Drop-formed vortex rings-the generation of vorticity, Phys. Fluids **7**, 1363 (1995).

[25] H. J. Lugt and S. Ohring, The oblique ascent of a viscous vortex pair toward a free surface, J. Fluid Mech. **236**, 461 (1992).

[26] T. Lundgren and P. Koumoutsakos, On the generation of vorticity at a free surface, J. Fluid Mech. **382**, 351 (1999).

[27] B. R. Morton, The generation and decay of vorticity, Geophys. Astrophys. Fluid Dynam. **28**, 277 (1984).

[28] S. J. Terrington, K. Hourigan, and M. C. Thompson, The generation and conservation of vorticity: Deforming interfaces and boundaries in two-dimensional flows, J. Fluid Mech. **890**, A5 (2020).

[29] S. J. Terrington, K. Hourigan, and M. C. Thompson, The generation and diffusion of vorticity in three-dimensional flows: Lyman's flux, J. Fluid Mech. **915**, A106 (2021).

[30] A. D. Dussaud and S. M. Troian, Dynamics of spontaneous spreading with evaporation on a deep fluid layer, Phys. Fluids **10**, 23 (1998).

[31] H. Kim, K. Muller, O. Shardt, S. Afkhami, and H. A. Stone, Solutal Marangoni flows of miscible liquids drive transport without surface contamination, Nat. Phys. **13**, 1105 (2017).

[32] H. Kim, J. Lee, T.-H. Kim, and H.-Y. Kim, Spontaneous Marangoni mixing of miscible liquids at a liquid-liquid-air contact line, Langmuir **31**, 8726 (2015).

[33] R. C. Ernst, C. H. Watkins, and H. H. Ruwe, The physical properties of the ternary system ethyl alcohol–glycerin–water, J. Phys. Chem. **40**, 627 (1936).

[34] J. Jeong and F. Hussain, On the identification of a vortex, J. Fluid Mech. **285**, 69 (1995).

[35] R. J. Adrian and J. Westerweel, *Particle Image Velocimetry* (Cambridge University, Cambridge, 2011).

[36] A. Agrawal and A. Prasad, Properties of vortices in the self-similar turbulent jet, Exp. Fluids **33**, 565 (2002).

[37] M. S. Chong, A. E. Perry, and B. J. Cantwell, A general classification of three-dimensional flow fields, Phys. Fluids A: Fluid Dyn. **2**, 765 (1990).

[38] R. Hain and C. Kähler, Fundamentals of multiframe particle image velocimetry (PIV), Exp. Fluids **42**, 575 (2007).

[39] J. Heyman, Tractrac: A fast multi-object tracking algorithm for motion estimation, Comput. Geosci. **128**, 11 (2019).

[40] J. C. R. Hunt, Eddies stream, and convergence zones in turbulent flows, Center for Turbulence Research CTR-S **88**, 193 (1988).

[41] G. S. H. Lock, *Latent Heat Transfer: An Introduction to Fundamentals* (Oxford University, New York, 1996).

[42] B. Wieneke, PIV uncertainty quantification from correlation statistics, Meas. Sci. Technol. **26**, 074002 (2015).

[43] Z. Xue, J. J. Charonko, and P. P. Vlachos, Particle image velocimetry correlation signal-to-noise ratio metrics and measurement uncertainty quantification, Meas. Sci. Technol. **25**, 115301 (2014).

[44] J. Zhou, R. J. Adrian, S. Balachandar, and T. M. Kendall, Mechanisms for generating coherent packets of hairpin vortices in channel flow, J. Fluid Mech. **387**, 353 (1999).